Inorganic Chemistry

Article

pubs.acs.org/IC

Effect of Ligand Substitution around the Dy^{III} on the SMM Properties of Dual-Luminescent Zn–Dy and Zn–Dy–Zn Complexes with Large Anisotropy Energy Barriers: A Combined Theoretical and Experimental Magnetostructural Study

Jean Pierre Costes,*[,†] Silvia Titos-Padilla,[‡] Itziar Oyarzabal,[§] Tulika Gupta,[⊥] Carine Duhayon,[†] Gopalan Rajaraman,*[,⊥] and Enrique Colacio*[,‡]

[†]Laboratoire de Chimie de Coordination, 205, route de Narbonne, Toulouse, 31077, France

[‡]Departamento de Química Inorgánica, Facultad de Ciencias, Universidad de Granada, Av. Fuentenueva S/N, 18071 Granada (Spain)

[§]Departamento de Química Aplicada, Facultad de Química, Universidad del País Vasco, UPV/EHU, Paseo Manuel Lardizabal, No. 3, 20018, Donostia-San Sebastián, Spain

[⊥]Department of Chemistry, Indian Institute of Technology—Bombay, Powai, Mumbai−400076, India

Supporting Information

ABSTRACT: The new dinuclear Zn^{II}–Dy^{III} and trinuclear Zn^{II}–Dy^{III}-Zn^{II} complexes of formula $[(LZnBrDy(ovan)(NO_3)(H_2O)](H_2O)\cdot 0.5(MeOH)$ (**1**) and $[(L^1ZnBr)_2Dy(MeOH)_2](ClO_4)$ (**3**) (L and L^1 are the dideprotonated forms of the *N*,*N*′-2,2-dimethylpropylenedi(3-methoxysalicylideneiminato and 2-{(*E*)-[(3-{[(2*E*,3*E*)-3-(hydroxyimino)-butan-2-ylidene]amino}-2,2-dimethylpropyl)imino]methyl}-6-methoxyphenol Schiff base compartmental ligands, respectively) have been prepared and magnetostructurally characterized. The X-ray structure of **1** indicates that the Dy^{III} ion exhibits a DyO_9 coordination sphere, which is made from four O atoms coming from the compartmental ligand (two methoxy terminal groups and two phenoxido bridging groups connecting Zn^{II} and Dy^{III} ions), other four atoms belonging to the chelating nitrato and ovanillin ligands, and the last one coming to the coordinated water molecule. The structure of **3** shows the central Dy^{III} ion surrounded by two L^1Zn units, so that the Dy^{III} and Zn^{II} ions are linked by phenoxido/oximato bridging groups. The Dy ion is eight-coordinated by the six O atoms afforded by two L^1 ligands and two O atoms coming from two methanol molecules. Alternating current (AC) dynamic magnetic measurements of **1**, **3**, and the previously reported dinuclear $[LZnClDy(thd)_2]$ (**2**) complex (where thd = 2,2,6,6-tetramethyl-3,5-heptanedionato ligand) indicate single molecule magnet (SMM) behavior for all these complexes with large thermal energy barriers for the reversal of the magnetization and butterfly-shaped hysteresis loops at 2 K. *Ab initio* calculations on **1**–**3** show a pure Ising ground state for all of them, which induces almost completely suppressed quantum tunnelling magnetization (QTM), and thermally assisted quantum tunnelling magnetization (TA-QTM) relaxations via the first excited Kramers doublet, leading to large energy barriers, thus supporting the observation of SMM behavior. The comparison between the experimental and theoretical magnetostructural data for **1**–**3** has allowed us to draw some conclusions about the influence of ligand substitution around the Dy^{III} on the SMM properties. Finally, these SMMs exhibit metal- and ligand-centered dual emissions in the visible region, and, therefore, they can be considered as magnetoluminescent bifunctional molecular materials.

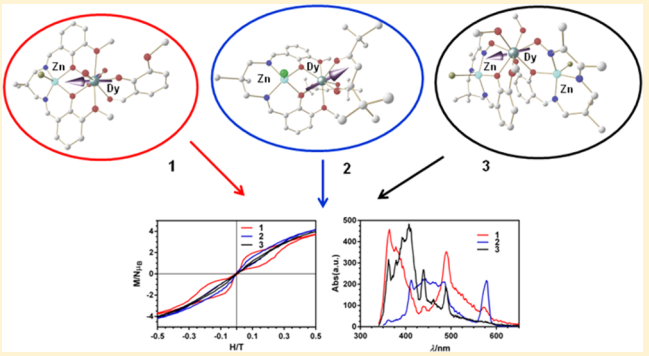

INTRODUCTION

Since the discovery, about two decades ago, of single molecule magnets (SMMs), which are molecular complexes exhibiting slow relaxation of the magnetization and magnetic hysteresis at low temperature, the research activity in the field has experienced impressive development, and a large number of SMMs have been reported so far.[1] SMMs are of current interest, not only because of their fascinating physical properties, such as freezing of the magnetization below the so-called "blocking temperature" (T_B), quantum tunnelling of the magnetization (QTM), and quantum phase interference,[1a] but also because of their potential future applications in fields such as molecular spintronics,[2] ultrahigh density magnetic information storage,[3] magneto-optics,[4] and as qubits for quantum computing at the molecular level.[5] One of the objectives of vast research activity in this field is the incorporation of SMMs in nanosized devices. The origin of

Received: January 28, 2016
Published: April 14, 2016

DOI: 10.1021/acs.inorgchem.6b00228
Inorg. Chem. 2016, 55, 4428−4440

Scheme 1. Preparation of Complexes 1−3

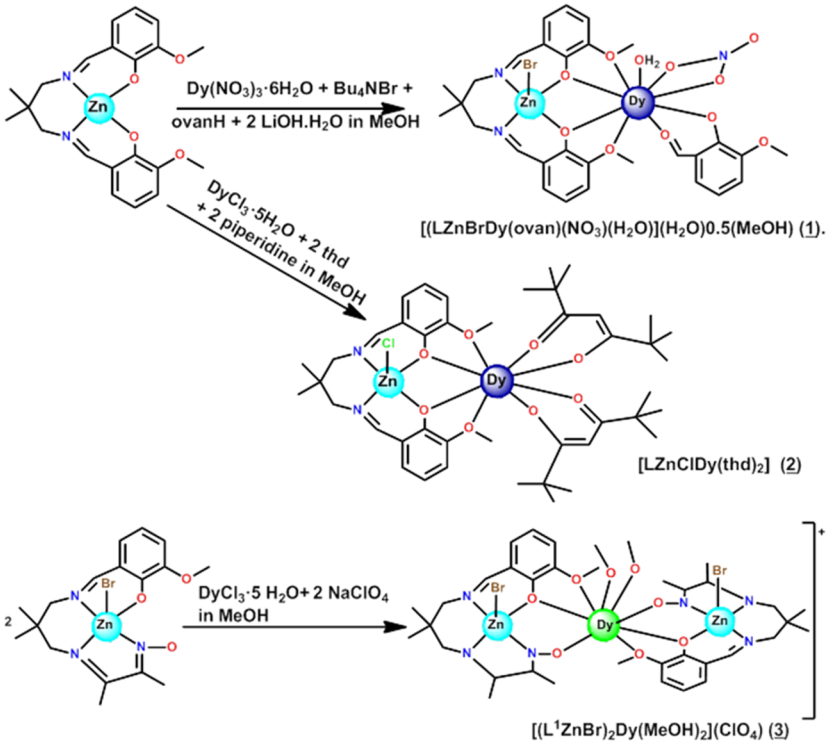

the SMM behavior is the existence of an energy barrier (U) for the reversal of the molecular magnetization (the energy required to convert a SMM in a paramagnet).[1a] Therefore, to observe SMM behavior at higher temperatures, the energy barrier should be as large as possible, which will lead to a concomitant increase of the relaxation time. Nevertheless, at present, the observed energy barriers are relatively low and therefore SMMs act as magnets at very low temperature.[1] It has been demonstrated that the magnetic anisotropy is the most important factor in determining the height of the energy barrier and therefore in the improvement of the SMM properties.[6] In view of this, highly anisotropic ions have been used to design SMMs with large thermal energy barriers. The first reported SMMs were clusters of transition-metal ions,[1u,v] the best example of them being a $\{Mn^{III}\}_6$ complex with an effective energy barrier U_{eff} = 62 cm^{-1} (Mn^{III} ions present a strong second-order spin−orbit coupling and, consequently, large ZFS).[7] Recently, also mononuclear transition-metal complexes of anisotropic metal ions such as Co^{II}, Fe^{I}, and Fe^{II} have been shown to exhibit SMM behavior at zero field.[1s] The best example of these systems is a linear Fe^{I} with large spin−orbit coupling and magnetic anisotropy which exhibit a large U_{eff} of 226 cm^{-1}.[8] Since lanthanide ions exhibit strong magnetic anisotropy, which arises from the combination of large magnetic moments, strong spin−orbit coupling and crystal-field effects, another important line research in this field is the use of lanthanide (and actinide) metal ions in designing SMMs.[1b−r] The aptness of this strategy has been demonstrated by the large number of 3d/4f low-nuclearity clusters and mononuclear 4f metal complexes that exhibit slow relaxation of the magnetization, most of them containing Dy^{III} ions.[1b−r] For 3d/4f systems, U_{eff} values as high as 82 cm^{-1} and observable hysteresis loops up to 3.7 K have been reported.[9,10] It is worth mentioning that mononuclear and low-nuclearity 4f metal complexes generally possess energy barriers that are an order-of-magnitude higher than observed 3d/4f polymetallic clusters, with U_{eff} and T_B (temperature at which the hysteresis opens) values as high as 652 cm^{-1} and 14 K, respectively.[11,12] In the former systems, the SMM behavior commonly is due to the individual Ln^{III} ions, rather than to the entire molecule, whereas in the latter, the height of the magnetization relaxation barrier is directly related to the 3d/4f magnetic exchange interactions. Thus, when the 3d/4f magnetic exchange coupling is strong, the exchange coupled levels are well-separated and the QTM is suppressed, so that large energy barriers and hysteresis loops are observed.[10,13] However, as the 3d/4f magnetic exchange couplings are generally weak, the separations between the low-lying split sublevels are small and consequently modest energy barriers for magnetization reversal are observed. In this regard, an effective and relatively easy approach to improve the SMM properties of the 3d/4f aggregates would be that of the removal of the very weak M^{II}−Ln^{III} interactions that split the ground sublevels of the Ln^{III} ion by substituting the paramagnetic M^{II} ions by diamagnetic ions. In fact, experimental results and theoretical calculations carried out by us and others[14] have shown that the incorporation of diamagnetic metal ions, such as Co^{III} and Zn^{II}, generally leads to higher U_{eff} than the MDy (M = Co and Ni) and homononuclear Dy counterparts. This phenomenon could be due to two factors: (i) the diminution of the intermolecular magnetic interactions provoked by the presence of diamagnetic ions (some type of magnetic dilution), which could reduce the faster QTM process that usually masks the slow relaxation process and the opening of the hysteresis loops at zero field in lanthanide containing complexes (although U_{eff} values of Ln-based species are very large infrequently show an open hysteresis loop at zero field) and (ii) the possible increase of electron density on the bridging oxygen donor atoms connecting the diamagnetic and Dy^{III} ions provoked by the coordination to the diamagnetic ion, which, in turn, induces a large electrostatic interaction with the

DOI: 10.1021/acs.inorgchem.6b00228
Inorg. Chem. 2016, 55, 4428−4440

lanthanide ion, giving rise to large separations of its crystal field levels and consequently to an increase of U_{eff}. This hypothesis was recently supported by theoretical calculations in Zn−Dy complexes.[14f] In this regard, it should be noted that the electron density and spatial arrangement of the oxygen donor atoms coordinated to the Dy^{III} play a decisive role in determining the SMM behavior of Dy-containing complexes. We and others have shown that the ligand substitution on the Dy coordination sphere and even more subtle changes as the replacement of counteranion have a great influence on the dynamic properties of 3d-Dy SMMs, where the 3d ion is diamagnetic (either Zn^{II} or Co^{III}).[14j,15]

We recently reported a series of Zn−Dy−Zn cationic complexes with the same N_2O_2 Schiff base compartmental ligand *N,N′*-2,2-dimethylpropylenedi(3-methoxysalicylideneiminato (H_2L) and double phenoxido bridging groups connecting Zn^{II} and Dy^{III} ions, which exhibited SMM behavior and large anisotropic barriers at zero field (97−147 K).[15] In all these complexes, which mainly differ in the co-ligands coordinated to the Zn^{II} ions (Cl^-, Br^-, H_2O) and counteranions (perchlorate or triflate), the Dy^{3+} ion exhibits a DyO_9 coordination sphere. Interestingly, the change of the co-ligand coordinated to the Zn^{2+} ion has a dramatic effect on the observed U_{eff} values. It would be of interest to analyze the effect on the SMM properties of these Zn−Dy−Zn complexes of (i) the replacement of the compartmental Schiff base ligand by another one having O atoms with different donor capability and (ii) the change of one of the ZnL fragments in the Zn−Dy−Zn complexes by O2-bidentate ligands affording Zn−Dy complexes. Along this line, we report here the syntheses, crystal structures, and detailed alternating current (AC) and direct current (DC) magnetic properties of two neutral Zn−Dy complexes ([(LZnBrDy(ovan) $(NO_3)(H_2O)$](H_2O)·0.5(MeOH) (**1**) and [LZnClDy$(thd)_2$] (**2**)) and a cationic trinuclear Zn−Dy−Zn complex ([$(L^1ZnBr)_2Dy(MeOH)_2$](ClO_4) (**3**) (H_2L^1 is 2-{(*E*)-[(3-{[(2*E*,3*E*)-3-(hydroxyimino)-butan-2-ylidene]amino}-2,2-dimethylpropyl)imino]methyl}-6-methoxyphenol) (see Scheme 1).

EXPERIMENTAL SECTION

Materials. The starting Schiff base zinc complex, LZn·$2H_2O$ (where L represents the *N,N′*-2,2-dimethylpropylenedi(3-methoxysalicylideneiminato) ligand), was prepared as previously described.[16] Preparations and crystal structures of the 1-(2,5,5-trimethylhexahydro-2-pyrimidinyl)-1-ethanone oxime ligand[17] and of the LZnClDy$(thd)_2$ complex[18] have been previously described. $DyCl_3·5H_2O$ and Dy$(NO_3)_3·5H_2O$ (Aldrich) were used as purchased. High-grade solvents, acetone (Normapur, VWR), methanol (Normapur, VWR), dichloromethane (laboratory reagent grade, Fisher) were used.

[Caution: perchlorates are potentially explosive and should be prepared only in small amounts and handled with care.]

*[(LZnBrDy(ovan) $(NO_3)(H_2O)$](H_2O)·0.5(MeOH) (**1**).* A mixture of LZn·$2H_2O$ (0.24 g, 5×10^{-4} mol) and Dy$(NO_3)_3·5H_2O$ (0.22 g, 5×10^{-4} mol), Bu_4NBr (0.16 g, 5×10^{-4} mol), ovanH (0.08 g, 5×10^{-4} mol), and LiOH·H_2O (0.04 g, 1×10^{-3} mol) in methanol (MeOH, 15 mL) was stirred for 30 min at room temperature and then filtered off. The solution was set aside and crystals that appeared 5 days later were filtered off and dried. Yield: 0.30 g (64%). Anal. Calcd for $C_{29.5}H_{37}BrDyN_3O_{12.5}Zn$ (941.42 g/mol): C, 37.64; H, 3.96; N, 4.46. Found: C, 37.42; H, 3.69; N, 4.31. IR (ATR, cm^{-1}): 3523m, 3459m, 2950w, 1632s, 1618s, 1548w, 1481w, 1459s, 1427s, 1408s, 1332w, 1314m, 1293s, 1243m, 1224m, 1210s, 1171m, 1079w, 1059m, 1023m, 960m, 926w, 850w, 742m, 728m, 640w.

*[L^1ZnBrNa] (**3′**).* A mixture of 1-(2,5,5-trimethylhexahydro-2-pyrimidinyl)-1-ethanone oxime (0.92 g, 5×10^{-3} mol) and of ovanillin (0.75 g, 5×10^{-3} mol) in MeOH was stirred and heated for 5 min, followed by the addition of $ZnBr_2$ (1.10 g, 5×10^{-3} mol), $CH_3COONa·3H_2O$ (1.00 g, 1×10^{-2} mol) and further heating for 20 min. The precipitate that appeared was cooled and filtered off, washed with cold MeOH and diethyl ether. Yield: 0.85 g (34%). Anal. Calcd for $C_{18}H_{27}BrN_3NaO_4Zn$ (517.71 g/mol): C, 41.76; H, 5.26 N, 8.12. Found: C, 41.36; H, 5.22; N, 8.23. IR (ATR, cm^{-1}): 3369m, 2957m, 2924m, 1633s, 1603m, 1546w, 1470m, 1449s, 1415m, 1370w, 1325m, 1240m, 1220s, 1167w, 1070m, 1020m, 974w, 856w, 787w, 751m, 668w, 645w.

*[(L^1ZnBr)$_2$Dy(MeOH)$_2$](ClO$_4$) (**3**).* A mixture of L^1ZnBrNa (0.10 g, 2×10^{-4} mol), $DyCl_3·5H_2O$ (0.07 g, 2×10^{-4} mol) and $NaClO_4$ (0.05 g, 4×10^{-4} mol) in methanol (30 mL) was stirred for 20 min and then filtered off. The solution was left aside and crystals that appeared 5 days later were filtered off and dried. Yield: 0.08 g (67%). Anal. Calcd for $C_{36}H_{54}Br_2ClDyN_6O_{12}Zn_2$ (1251.40 g/mol): C, 34.55; H, 4.35 N, 6.72. Found: C, 34.25; H, 4.21; N, 6.53. IR (ATR, cm^{-1}): 3371m, 2965m, 2944m, 1639m, 1627s, 1608m, 1566w, 1469s, 1435m, 1416m, 1393w, 1367w, 1292m, 1282m, 1244w, 1223s, 1170w, 1078m, 1062s, 1019m, 967w, 928w, 847w, 780w, 735m, 641w, 621w.

Physical Measurements. Elemental analyses for C, H, and N were performed at Microanalytical Laboratory of the Coordination Chemistry Laboratory in Toulouse, France. IR spectra were recorded with a PerkinElmer Spectrum 100FTIR, using the ATR mode. Magnetic data were obtained with Quantum Design MPMS SQUID XL-5 susceptometer and Physical Properties Measurement System PPMS 6000. All samples were 3-mm-diameter pellets molded from ground crystalline samples. Magnetic susceptibility measurements were performed in the 2−300 K temperature range in a 0.1 T applied magnetic field, and diamagnetic corrections were applied by using Pascal's constants. Isothermal magnetization measurements were performed up to 5 T at 2 K. AC susceptibility measurements under different applied static fields were performed using an oscillating AC field of 3.5 Oe and AC frequencies ranging from 10 Hz to 10000 Hz.

Crystallographic Data Collection and Structure Determination for Complexes 1 and 3. Crystals of **1** and **3** were kept in the mother liquor until they were dipped into oil. The chosen crystals were mounted on a Mitegen micromount and quickly cooled to 180 K (**1**) or 100 K (**3**). The selected crystals of **1** (yellow, 0.20 mm × 0.20 mm × 0.25 mm), **3** (colorless, 0.30 mm × 0.10 mm × 0.05 mm) were mounted on an Oxford-Diffraction Gemini (**3**) or a Bruker Kappa Apex II (**1**), using a graphite monochromator (λ = 0.71073 Å), and equipped with an Oxford Cryosystems cooler device. The unit-cell determination and data integration were carried out using CrysAlis RED or SAINT packages.[19−21] The structures have been solved using SUPERFLIP[22] and refined by least-squares procedures using the software package CRYSTALS.[23] Atomic scattering factors were taken from the *International Tables for X-ray Crystallography*.[24] Hydrogen atoms were refined by using a riding model. All non-hydrogen atoms were anisotropically refined. Treatment with the SQUEEZE facility from PLATON[25] for **3** resulted in a smooth refinement. Since a few low-order reflections are missing from the dataset, the electron count is underestimated. Thus, for complex **3**, the values given for D(calc), F(000), and the molecular weight are only valid for the ordered part of the structure. Drawings of molecules are performed with the program CAMERON.[26]

*Crystal Data for **1**.* $C_{29.5}H_{37}BrDyN_3O_{12.5}Zn$, M = 939.39, orthorhombic, *Pbca*, Z = 8, a = 18.6397(5) Å, b = 12.4461(3) Å, c = 30.7444(9) Å, $\alpha = \beta = \gamma = 90°$, V = 7132.4(3) Å^3, 131 903 collected reflections, 9485 unique reflections (R_{int} = 0.0267), 442 parameters, R-factor = 0.041, weighted R-factor = 0.039 for 7797 contributing reflections [$I > 3\sigma(I)$].

*Crystal Data for **3**.* $C_{36}H_{55}Br_2ClDyN_6O_{12}Zn_2$, M = 1252.39, monoclinic, $P2_1/c$, Z = 4, a = 8.39264(12) Å, b = 29.4811(5) Å, c = 20.2037(3) Å, β = 93.7377(13)°, V = 4988.24(12) Å^3, 12 689 collected reflections, 12 693 unique reflections (R_{int} = 0.055), 559 parameters, R = 0.061, R_w = 0.062 for 9550 contributing reflections [$I > 3\sigma(I)$].

Computational Methodology. MOLCAS 8.0 program package has been used to perform post-Hartree−Fock *ab initio* calculations.[27]

DOI: 10.1021/acs.inorgchem.6b00228
Inorg. Chem. 2016, 55, 4428−4440

Using a multiconfigurational approach, relativistic effects were treated in two steps, based on the Douglas–Kroll Hamiltonian. For the generation of basis sets, scalar terms were included that has been used to determine spin-free wave functions and also energies through the use of the complete active space self-consistent field (CASSCF) method.[28] So, spin–orbit free states were obtained by employing the RASSCF method, whereas spin–orbit coupling has been taken into account using RASSI-SO method,[29] which uses CASSCF wave functions as the basis sets and multiconfigurational wave functions as input states. The resulting wave functions and the energies of the molecular multiplets were used for the calculation of the magnetic properties and *g*-tensors of the lowest state using a specially designed SINGLE-ANISO routine.[30] As a consequence, the magnetic properties of a single magnetic ion are calculated by a fully *ab initio* approaching which the spin–orbit coupling is considered nonperturbatively. We have employed the [ANO-RCC···7s6p4d2f][31] basis set for Dy^{III}, the [ANO-RCC···3s2p] basis set for N, the [ANO-RCC···3s2p] basis set for O, the [ANO-RCC···5s4p2d] basis set for Zn, and the [ANO-RCC···2s] basis set for H throughout our calculations. These ANO-RCC-VDZ basis sets, which are used for all of the atoms, are taken from ANO-RCC basis library included in MOLCAS 7.8 program package.

RESULTS AND DISCUSSION

Synthetic Aspects. Compounds **1**–**3** were synthesized following the "complex-as-ligand" approach, using the mononuclear Zn^{II} complexes $LZn{\cdot}2H_2O$ and $[L^1ZnBrNa]$ as building blocks to be assembled with the Dy^{III} ion and the corresponding bidentate ligands. Thus, the reaction of $LZn{\cdot}2H_2O$ with $Dy(NO_3)_3{\cdot}5H_2O$, Bu_4NBr, ovanH (ortho-vanillin), and $LiOH{\cdot}H_2O$ in MeOH and using a 1:1:1:1:2 molar ratio afforded complex **1**, wheras the reaction of $LZn{\cdot}2H_2O$ with tetramethylheptanedione (thd), $DyCl_3{\cdot}6H_2O$, and piperidine in MeOH and using a 1:2:1:2 molar ratio gave rise to complex **2**. Complex **3** was obtained from the reaction of $L^1ZnBrNa$, $DyCl_3{\cdot}5H_2O$, and $NaClO_4$ in MeOH and using a 1:1:2 molar ratio (see Scheme 1).

Crystal Structures. Complex **1** crystallizes in the orthorhombic *Pbca* space group with $Z = 8$. The crystallographic data appear in the experimental part. The asymmetric unit of **1** is represented in Figure 1, and selected bonds and angles are given in the corresponding figure caption. The single-crystal X-ray structure of complex **1** corroborates that we are dealing with a dinuclear Zn–Dy entity in which the Zn ion occupies the inner N_2O_2 coordination site and the Dy ion occupies the outer O_2O_2 coordination site of the compartmental Schiff base ligand. The Zn^{II} and Dy^{III} metal ions are bridged by the two deprotonated phenoxido O atoms and the four ZnO_2Dy atoms are not coplanar, with the dihedral angle between the Zn–O1–O2 and Dy–O1–O2 planes being equal to 6.8(1)°. The central core of the molecule is characterized by very similar Zn–O(*i*) (*i* = 1, 2) (2.080(2) and 2.053(2) Å) and Dy–O(*i*) bond lengths (2.302(2) and 2.329(2) Å) and similar Zn–O(*i*)-Dy angles (108.2(1)°), giving a Zn–Dy distance of 3.5531(4) Å. The Zn ion is in a square pyramidal environment, the N_2O_2 atoms of the ligand defining the basal plane while the bromide ion occupies the apical position with a longer Zn–Br bond (2.5011(5) Å). The Zn ion is located 0.4906(4) Å above the mean N_2O_2 basal plane. There is an intramolecular hydrogen bond between the Br ion and the water molecule coordinated to the Dy ion and the shortest Dy···Dy distance is equal to 8.910(1) Å. The Dy^{III} ion is nine-coordinated, four oxygen atoms coming from the main ligand and four from the chelating nitrato and ovanillin ligands, and the last one from the coordinated water molecule. As usual, the Dy–O methoxy

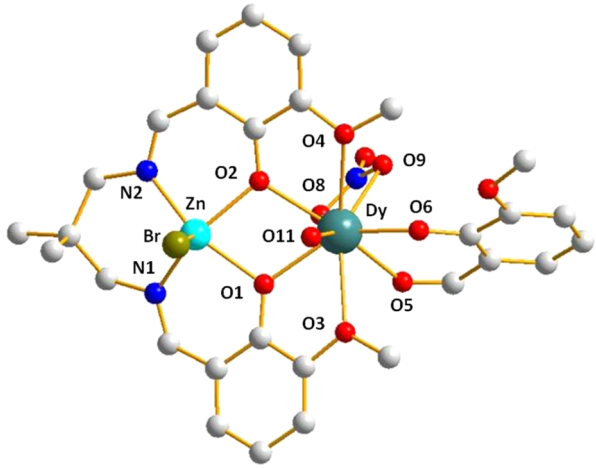

Figure 1. Molecular structure for **1**. Selected bond lengths and distances: Zn–N1, 2.065(3) Å; Zn–N2, 2.065(3) Å; Zn–O1, 2.080(2) Å; Zn–O2, 2.053(2) Å; Zn–Br, 2.5011(5) Å; Dy–O1, 2.302(2) Å; Dy–O2, 2.329(2) Å; Dy–O3, 2.581(3) Å; Dy–O4, 2.565(2) Å; Dy–O5, 2.412(3) Å; Dy–O6, 2.213(2) Å; Dy–O8, 2.507(3) Å; Dy–O9, 2.474(3) Å; and Dy–O11, 2.393(3) Å. Selected bond angles: Zn–O1–Dy, 108.2(1)°, Zn–O2–Dy, 108.2(1)°.

bond lengths are largest (2.581(3) and 2.565(2) Å) than the Dy–O nitrate bond lengths (2.507(3)-2.474(3) Å), the Dy–O aldehyde from ovan (2.412(3) Å) and the water Dy–O bond (2.393(3) Å). The phenoxido Dy–O bond from the ovan ligand is shorter (2.213(2) Å) than those from the main ligand (2.302(2) and 2.329(2) Å). The angle between the mean N_2O_2 plane and the plane defined by the Dy^{III} ion and the chelating ovan ligand is equal to 50.95(7)°.

Note that the structure of **1** is very similar to that previously reported for the analogous complex $[(LZnBrDy(sal)(NO_3)(H_2O)]$ (Hsal = salycilaldehyde).[14a]

Complex **3** crystallizes in the monclinic $P2_1/c$ space group with $Z = 4$. The crystallographic data appear in the experimental part. The cationic trinuclear network represented in Figure 2 corresponds to the formula $[(L^1ZnBr)_2Dy(MeOH)_2]^+$, which a perchlorate anion, ensuring electroneutrality. There are few differences between the bond lengths and bond angles of the two (L^1ZnBr) moieties, but the cation has no crystallographic symmetry. In comparison to the previous structure, the Zn ions, which have a classical square-pyramidal environment, are chelated to a nonsymmetric Schiff base ligand furnishing the four basal N_3O donor atoms, with a Br ion occupying the apical position. The Zn–Br bond lengths are shorter than in **1** (2.357(1) and 2.407(1) Å) while the Zn–N (imine) of the butanemonoxime part of the ligand (2.170(5) and 2.146(5) Å) are longer than the other Zn–N bonds (2.044(5)–2.098(5) Å). The central Dy ion is linked to each Zn ion by a double (O, N–O) bridge (O standing for the phenolato O atom and N–O for the oximato group of the L^1 ligand). The five atoms involved in each Zn(O, N–O)Gd bridge are not exactly coplanar. The hinge angles between the (OZnN) and (ODyO) planes are equal to 10.8(1)° and 11.9(1)° in the Zn(1) and Zn(2) moieties, respectively. The intramolecular Zn···Dy distances are equal to 3.8582(6) Å and 3.8917(6) Å, with a Zn1···Zn2 distance of 6.8467(9) Å. The Dy ion is eight-coordinated. In addition to the six O atoms afforded by two L^1 ligands, the rare-earth ion achieves its environment with two O atoms coming from two methanol molecules. As previously noted, the Dy–O bond lengths are dependent on

DOI: 10.1021/acs.inorgchem.6b00228
Inorg. Chem. 2016, 55, 4428–4440

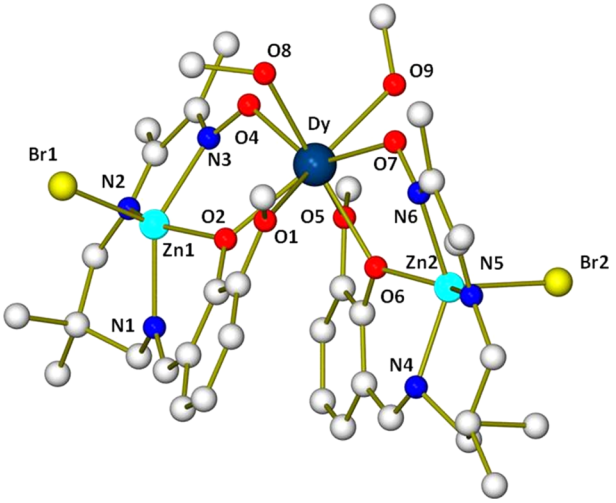

Figure 2. Molecular structure for **3**. Selected bond lengths and distances: Zn1–N1, 2.044(5) Å; Zn1–N2, 2.170(5) Å; Zn1–N3, 2.063(4) Å; Zn1–O2, 2.085(4) Å; Zn1–Br1, 2.357(1) Å; Zn2–N4, 2.087(6) Å; Zn2–N5, 2.146(5) Å; Zn2–N6, 2.098(5) Å; Zn2–O6, 2.069(3) Å; Zn2–Br2, 2.407(1) Å; Dy–O1, 2.528(4) Å; Dy–O2, 2.312(4) Å; Dy–O4, 2.310(4) Å; Dy–O5, 2.486(3) Å; Dy–O6, 2.347(4) Å; Dy–O7, 2.274(4) Å; Dy–O8, 2.371(4) Å; Dy–O9, 2.386(4) Å. Selected bond angles: Zn1–N3–O4, 122.9(3)°; Zn2–N6–O7, 122.7(3)°; Zn1–O2–Dy, 122.6(2)°; Zn2–O6–Dy, 123.5(2)°; Dy–O4–N3, 120.9(3)°; and Dy–O7–N6, 119.6(3)°.

the nature of the O atoms; they vary from 2.274(4) Å to 2.528(4) Å. The bonds issued from the oximato (2.274(4)–2.310(4) Å) and phenolato oxygens (2.312(4)–2.347(4) Å) are shorter than those from the methanol molecules (2.371(4)–2.386(4) Å), with the largest ones being related to the methoxy side arms (2.486(3)–2.528(4) Å). The two L^1ZnBr units are disposed in a head-to-tail arrangement around the Dy ion, moved back (rotated by) 87.5(1)°. The main N3O basal planes are not parallel, making an angle of 24.2(1)°, so that the Zn–Dy–Zn ions are not aligned, with an angle of 124.1(1)°. There are no intramolecular or intermolecular hydrogen bonds, and the shortest intermolecular Dy···Dy distance is large, equal to 10.544(1) Å.

The main differences between the trinuclear **3** and binuclear **1** complexes originate in the nature of the actual polynuclear species (cationic vs neutral) and the coordination number of the Dy ion (eight vs nine). Note that the structure of the neutral complex [LZnClDy(thd)$_2$] (**2**) (Figure 3), which was recently reported by two of us,[18] is similar to that of **1**; however, the Dy ion exhibits a DyO_8 coordination environment, which is formed by the coordination of the two phenoxido and two methoxy O atoms from the ligand and four O atoms belonging to two tetramethylheptanedione bidentate ligands. Moreover, there is a chloride anion coordinated in the apical position of the square-pyramidal Zn^{II} ions instead of the bromide ligand observed in **1**.

The calculation of the degree of distortion of the DyO_9 coordination polyhedron for **1** and the DyO_8 coordination polyhedron for **2** and **3**, with respect to ideal nine- and eight-vertex polyhedra, respectively, by using the continuous shape measure theory and SHAPE software,[32] show the following:

(i) The DyO_9 arrangement for **1** is intermediate between various coordination polyhedral (Table S1 in the Supporting Information). The lowest shape measures correspond to Muffin (MFF-9), spherical capped square antiprism (CSAPR-9), and spherical tricapped trigonal prism (TCTPR-9), with values of 0.992, 2.088, and 2.459, respectively.

(ii) The lowest shape measures for the DyO_8 coordination environment in **2** belong to biaugmented trigonal prism (BTPR-8), biaugmented trigonal prism J50(JBTPR-8), and triangular dodecahedron (TDD-8), with values of 1.907, 2.090, and 2.990, respectively.

(iii) For **3**, the lowest values correspond to trigonal dodecahedron (TDD-8), square antiprism (SAPR-8), and biaugmented trigonal prism (BTPR-8) with values of 1.060, 1.259, and 2.172, respectively.

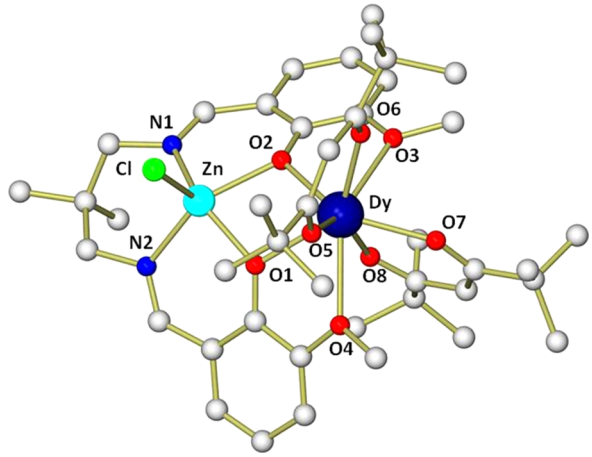

Figure 3. Molecular structure for **2**. Selected bond lengths and distances: Zn–N1, 2.071(3) Å; Zn–N2, 2.094(2) Å; Zn–O1, 2.056(2) Å; Zn–O2, 2.101(2) Å; Zn–Cl, 2.2584(9) Å; Dy–O1, 2.350(2) Å; Dy–O2, 2.336(2) Å; Dy–O(OMe), 2.552(2)–2.558(2) Å; Dy–O(thd), 2.266(2)–2.292(2) Å. Selected bond angles: O1–Zn–O2, 77.26 (7)°; O1–Dy–O2, 67.28(7)°; Zn–O1–Dy, 104.72(8)°; and Zn–O2–Dy, 103.74(8)°.

The coordination polyhedra with the lowest shape measures for **1**–**3**, together with the shorter Dy–O distances are given in Figure 4.

Magnetic Properties. The temperature variation of the direct-current (DC) magnetic susceptibility (χ_M) for **1**–**3** were recorded in a 1000 Oe applied field between 300 K and 2 K and are given in Figure 5 (complex **1**) and Figures S1 and S2 in the Supporting Information (complexes **2** and **3**, respectively) in the form $\chi_M T$ vs T.

The room-temperature $\chi_M T$ value for **1**–**3** of 14.38, 14.16, and 14.02 cm^3 K mol^{-1} at 300 K are compatible with the expected value of 14.17 cm^3 K mol^{-1} for one Dy^{3+} ion ($4f^9$, J = 15/2, S = 5/2, L = 5, g = 4/3, $^6H_{15/2}$) in the free-ion approximation. Upon cooling, the $\chi_M T$ product for **1** steadily decreases to reach a value of 12.03 cm^3 at 2 K. For **2** and **3**, the $\chi_M T$ product remains almost constant to 100 K, then continuously decreases down to 20 K and finally drops off abruptly to reach values of 12.56 cm^3 K mol^{-1} and 10.58 cm^3 K mol^{-1}, respectively. This behavior is caused by the depopulation of the excited m_j sublevels of Dy ions, which emerge from the splitting of the $^6H_{15/2}$ ground term by the ligand field, and/or possible very weak intra/intermolecular interactions between the Dy^{3+} ions. The field dependence of the magnetization for **1**–**3** at 2 K shows a relatively rapid increase in the magnetization to almost reach the saturation for magnetic fields of >2 T. The saturation values of 5.0 Nμ_B, 5.15 Nμ_B, and 5.21 Nμ_B for **1**–**3**, respectively, are rather lower than that

DOI: 10.1021/acs.inorgchem.6b00228
Inorg. Chem. 2016, 55, 4428–4440

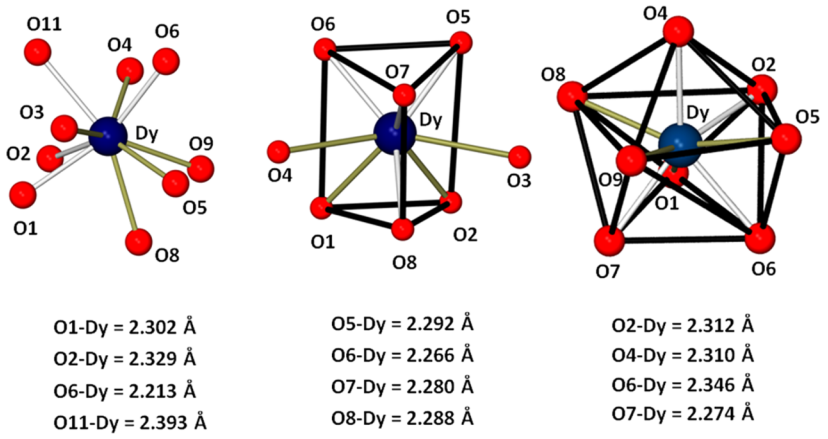

Figure 4. Coordination polyhedra with lowest shape measures and the four shortest Dy–O distances (silver color) for complexes **1**–**3** (from left to right).

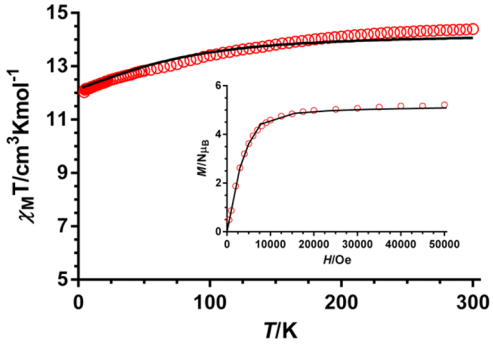

Figure 5. Temperature dependence of $\chi_M T$ for **1** (inset shows the field dependence of molar magnetization for **1**). Solid lines correspond to the curves generated from *ab initio* results.

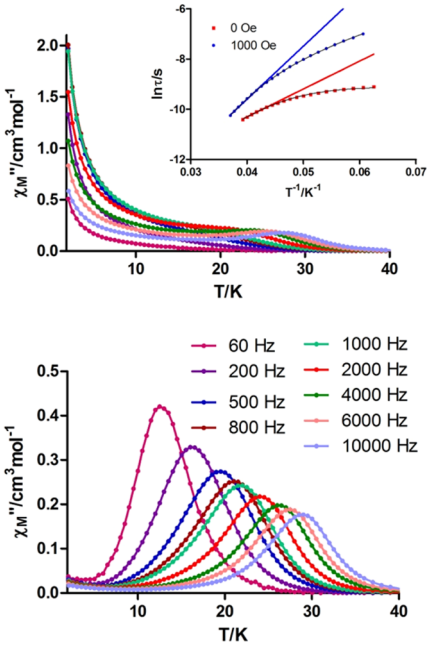

Figure 6. Temperature dependence of out-of-phase susceptibility signals at zero (top) and 1000 Oe (bottom) applied dc field for complex **1**. Inset shows Arrhenius plots for the relaxation times (τ) in zero (red solid line) and 1000 Oe (blue solid line) applied DC fields for complex **1**. The black solid lines represent the best fits to Orbach plus QTM (red solid squares, data at zero DC field) and to Orbach plus Raman (blue solid circles, data at 1000 Oe).

expected for one Dy^{3+} of 10 Nμ_B (Ms/Nμ_B = $g_J J$ = 10 Nμ_B), which is due to significant magnetic anisotropy arising from the crystal-field effects.[14]

The $\chi'_M T$ for **1**–**3** (with an alternating field of 3.2 Oe; see below) at its low temperature plateau (at zero and 1000 Oe) takes a value close to 12.5 cm^3 mol^{-1} K, the expected value for randomly oriented crystals with a m_j = ±15/2 pure axial Kramers doublet. Therefore, the anticipated easy-axis anisotropy of the Dy^{III} ion in these compounds should favor the slow relaxation of the magnetization and the SMM behavior. Dynamic alternating-current (AC) magnetic susceptibility measurements, as a function of both temperature and frequency, were performed on **1**–**3** with the aim of knowing whether or not they exhibit SMM properties. In zero-applied DC magnetic field (Figures 6–8 (insets) and Figures S3–S5 in the Supporting Information), the three compounds display frequency dependence of the out-of-phase susceptibility (χ''_M) with peaks at 27, 18, and 14 K at the highest used frequency (10 000 Hz) for **1**, **2**, and **3**, respectively, thus indicating that they present slow relaxation for the reversal of magnetization and SMM behavior. The peaks at high temperature overlap with tails at low temperature (χ''_M does not go to zero below the maxima but increases at very low temperature), which is a clear sign of fast QTM. For Kramers ions, such as Dy^{III}, with easy-axis anisotropy, dipole–dipole and hyperfine interactions allow the mixing of the two Kramers ground states at zero DC field, thus promoting the quantum tunneling dynamics of the magnetization. In fact, the Cole–Cole plots (Figure S4) in the temperature ranges of 2–25 K for **1**, 2–16 K for **2**, and 2–14 K for **3** exhibit semicircular shapes with α parameters in the ranges of 0.21–0.02, 0.18–0.14, and 0.26–0.06, respectively, corroborating the existence of multiple relaxation processes.

The dependence of χ''_M on the frequency at each temperature was fitted to the generalized Debye model (Figure S5), which allowed the relaxation times τ to be extracted. The fitting of τ to the Arrhenius law afforded the U_{eff} values listed in Table 1. As the deviation of the data from linearity is mainly due to QTM (see Figures 6–8), the relaxation times were fitted to the following equation, where relaxation through both quantum tunnelling and Orbach thermal processes are considered:

DOI: 10.1021/acs.inorgchem.6b00228
Inorg. Chem. 2016, 55, 4428–4440

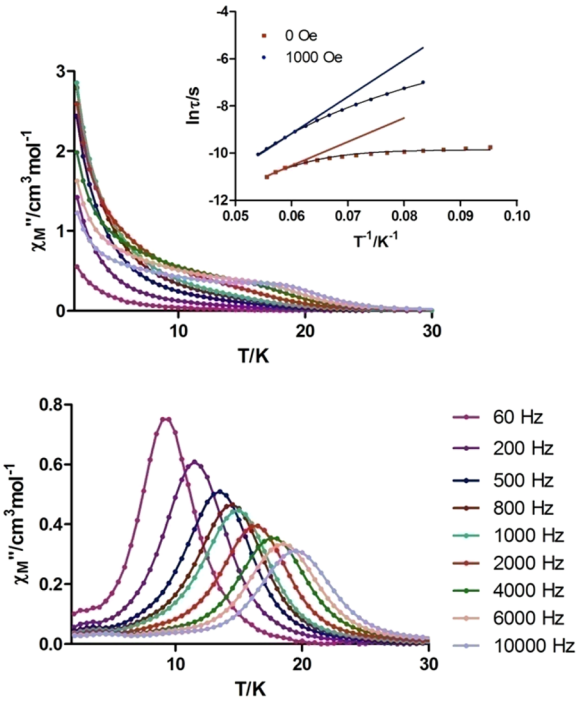

Figure 7. Temperature dependence of out-of-phase susceptibility signals at zero (top) and 1000 Oe (bottom) applied DC field for complex **2**. Inset shows Arrhenius plots for the relaxation times (τ) (red solid line) and 1000 Oe (blue solid line) applied DC fields for complex **2**. The black solid lines accounts for the best fits to Orbach plus QTM (red solid squares, data at zero dc field) and to Orbach plus Raman (blue solid circles, data at 1000 Oe).

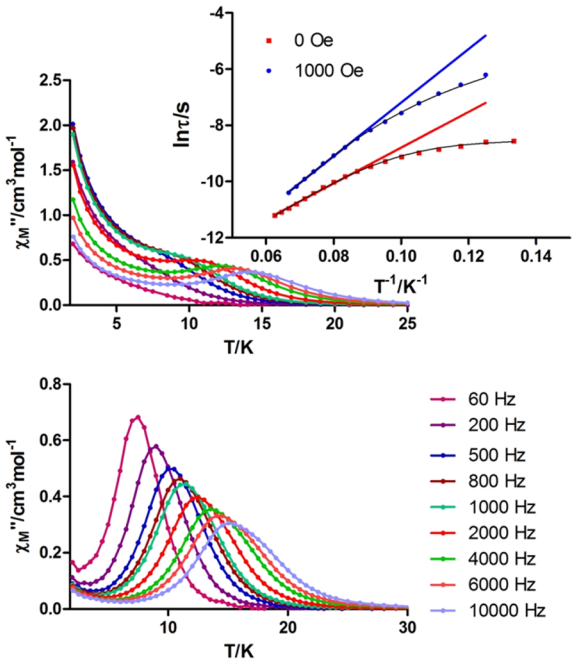

Figure 8. Temperature dependence of out-of-phase susceptibility signals at zero (top) and 1000 Oe (bottom) applied DC field for complex **3**. Inset shows Arrhenius plots for the relaxation times (τ) in zero (red solid line) and 1000 Oe (blue solid line) applied DC fields for complex **3**. The black solid lines account for the best fits to Orbach plus QTM (red solid squares, data at zero DC field) and to Orbach plus Raman (blue solid circles, data at 1000 Oe).

$$\tau^{-1} = {\tau_{QTM}}^{-1} + {\tau_0}^{-1} \exp\left(-\frac{U_{eff}}{k_B T}\right)$$

The fit of the data led to higher U_{eff} values and lower flipping rates (τ_0) than the simple Arrhenius law, which are indicated in Table 1, together with τ_{QTM} values.

In the presence of an external DC magnetic field (H_{dc}) of 1000 Oe, the QTM was quenched and, consequently, the tails at low temperatures almost disappeared, giving rise to well-defined out-of-phase susceptibility peaks in the temperature ranges of 12−28 K, 9−19.5 K, and 7.5−15 K (60−10000 Hz), respectively for **1**−**3** (Figures 6−8 and Figures S6−S8 in the Supporting Information). The high-temperature relaxation times were fitted to the Arrhenius law, leading to an augmentation of the thermal energy barrier and a reduction of $\tau_{0,}$ as expected (see Table 1). However, the experimental relaxation times do not follow the linear Arrhenius model below 14−15 K, even though the QTM is almost suppressed after the application of an external magnetic field. The Cole−Cole plots (Figure S7) with α values in the ranges of 0.06 (15 K) to 0.05 (28 K), 0.13 (11 K) to 0.12 (19 K), and 0.15 (9 K) to 0.12 (15.5 K) for **1**−**3**, respectively, indicate the presence of a distribution of relaxation processes in the low-temperature region. The observed behavior may indicate the existence of competing Orbach and Raman processes; therefore, we have fitted the experimental data to the following equation, which includes contributions of both relaxation processes.

$$\tau^{-1} = BT^n + {\tau_0}^{-1} \exp\left(-\frac{U_{eff}}{k_B T}\right)$$

The first term corresponds to the Raman process, while the second term accounts for the Orbach process. Although a value of $n = 9$ is expected for Kramers ions,[33] n values in the range of 1−6 can be considered to be reasonable.[14c,34] The best fit of the experimental data led to higher thermal energy barriers (Table 1), which seems to indicate that the Raman relaxation process significantly influences the Orbach relaxation process, decreasing the thermal energy barrier U_{eff} for the magnetization reversal.

***Ab Initio* Calculations.** The energy spectrum and g-tensors for the Kramers doublets of the ground $^6H_{15/2}$ multiplet of the Dy^{III} ion in compounds **1**−**3** are shown in Table 2 (see also Tables S2−S4 in the Supporting Information). Note that subsequent excited states are located at 3080, 3090, and 3070 cm^{-1} for **1**, **2**, and **3**, respectively.

In all of the complexes, the ground-state anisotropy is of pure Ising type, indicating a large magnetic moment with g_z approaching toward ideally pure $m_J = \pm 15/2$ state ($g_z = 20$). Moreover, the ground-state QTM is nonoperative, because of the almost-zero transverse magnetic moment (10^{-1} magnitude order of transverse anisotropy, which significantly reduces the QTM probability). Axiality of the excited states decreases until the seventh, sixth, and fifth Kramers doublet (KD) for **1**, **2**, and **3**, respectively, with a proportional increase of magnetic moment along the XY plane (increase of transverse anisotropy components).

The calculated orientations of the magnetic moments of the ground state for **1**−**3** (see Figure 9, as well as Figure S9 in the Supporting Information) lie close to the shortest Dy−O bonds, as expected from the electrostatic simple oblate−prolate model.[35] In fact, the orientations of the anisotropy axis for **1**−**3**, calculated using a simple quantitative electrostatic

DOI: 10.1021/acs.inorgchem.6b00228
Inorg. Chem. 2016, 55, 4428−4440

Table 1. Fitting Parameters for Orbach, QTM, and Raman Processes for Compounds 1−3

	H = 0 Oe					H = 1000 Oe					
	Orbach		Orbach + QTM			Orbach		Orbach + Raman			
compound	U_{eff} (cm^{-1})	τ_0 (s)	U_{eff} (cm^{-1})	τ_0 (s)	τ_{QTM} (s)	U_{eff} (cm^{-1})	τ_0 (s)	U_{eff} (cm^{-1})	τ_0 (s)	b	n
1	82.9	2.8×10^{-7}	118.1	5.3×10^{-8}	1.1×10^{-4}	146.7	1.5×10^{-8}	233.7	2.6×10^{-10}	0.001	5.1
2	69.3	5.2×10^{-8}	108.0	3.9×10^{-9}	3.7×10^{-5}	111.5	5.5×10^{-9}	156.3	2.9×10^{-10}	0.001	5.5
3	44.3	2.6×10^{-7}	55.6	9.5×10^{-8}	1.9×10^{-4}	66.4	5.4×10^{-8}	82.8	1.5×10^{-8}	0.05	4.4

Table 2. Calculated Energy Spectrum, *g*-Tensors, and Angles (θ) of the Principal Anisotropy Axes of the First, Second, and Third Excited State (KD1, KD2, and KD3, Respectively), with Respect to the Ground State (GS) for Complexes 1, 2, and 3, Respectively

	energy (cm^{-1})	g_{xx}	g_{yy}	g_{zz}	θ (deg)
1-KD1	0.0	0.0	0.0	19.94	
2-KD1	0.0	0.02	0.03	19.73	
3-KD1	0.0	0.01	0.02	19.71	
1-KD2	177.5	0.14	0.19	16.92	6.0
2-KD2	159.9	0.43	0.79	15.64	2.7
3-KD2	131.3	0.10	0.11	16.73	8.8
1-KD3	302.2	1.31	1.48	13.39	7.6
2-KD3	228.6	0.01	0.69	14.11	145.1
3-KD3	267.8	0.20	0.33	13.49	6.4

approach, compare well with that obtained by *ab initio* calculations.[14f,15,36] In the case of **1**, the orientation of the magnetic moment can be explained by the fact that the Dy−O distance (Dy−O6 = 2.213 Å) is significantly shorter (more than 0.1 Å) than the other ones. The *f* electron density of the m_J = ±15/2 Kramers doublet ground state of the Dy^{III} center possesses an oblate shape, and, to reduce the repulsion with the closest coordinated atom, the electron density disk is situated almost perpendicular to the shortest Dy−O bond. Therefore, the anisotropy axis is perpendicular to the electron density disk and, consequently, lies along the direction of the shortest Dy−O bond (see Figure 9). This assumption is supported by our computed Mulliken charges, where O6 atoms have a significantly large negative charge, compared to other O atoms, barring only the μ-phenoxido O atoms (see Figure 10a). The large charge on the phenoxido O atom is due to the coordination of this atom with the diamagnetic Zn^{2+} cation, as illustrated earlier by us and others.[14c,f,g,37]

In complexes **2** and **3**, the differences between the shortest Dy−O bond distances are much smaller than in **1**. Nevertheless, in the DyO_8 coordination sphere of **2** and **3** (see Figure 4), there are large negatively charged O atoms with short Dy−O distances at opposite sides of the Dy^{III} ion (5, 6, 7, and 8 are keto oxygen atoms, 1 and 2 are oxime oxygens, 3 and 4 are phenoxido oxygen atoms for **2**, as per Figure 11, and 11, 12, 13, 14, 15, 16, 17, and 18 are O atoms for **3**, as per Figure 12). DFT-computed Mulliken charge analysis reveals that negative charge ligand field created by Dy^{III}-coordinated O atoms is much stronger for **2**/**3**, compared to **1**. This is essentially due to

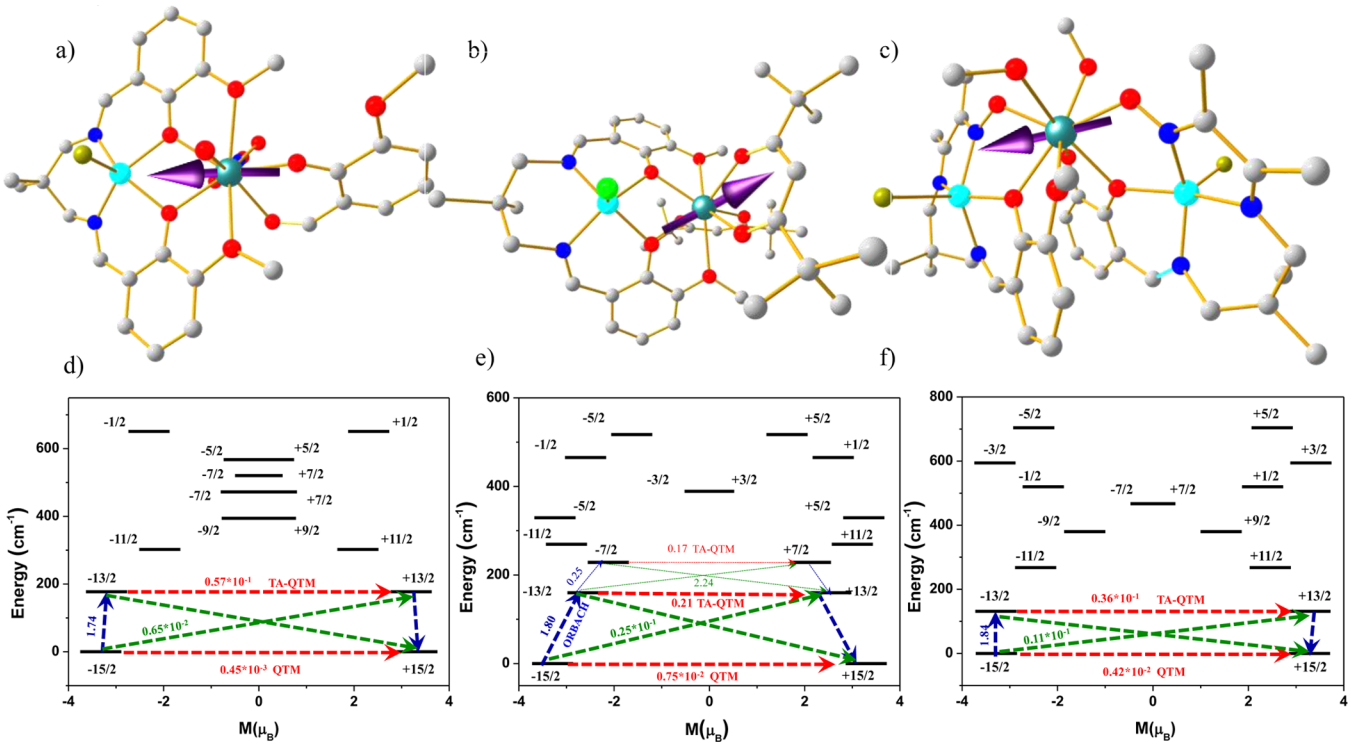

Figure 9. *Ab initio* computed ground-state principal anisotropy direction (g_{zz}) for complexes (a) **1**, (b) **2**, and (c) **3**; *ab initio* computed relaxation mechanism in (d) **1**, (e) **2**, and (f) **3**.

DOI: 10.1021/acs.inorgchem.6b00228
Inorg. Chem. 2016, 55, 4428−4440

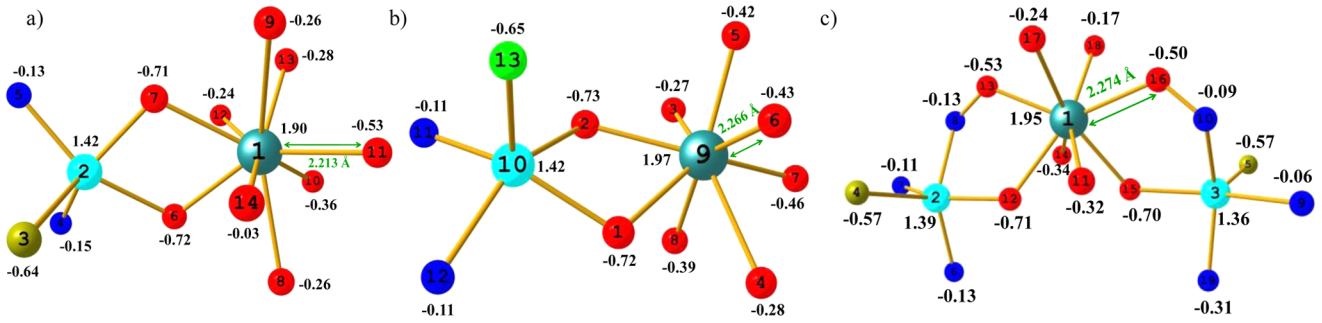

Figure 10. Density functional theory (DFT)-computed Mulliken charges on the donor atoms of complex (a) **1**, (b) **2**, and (c) **3**.

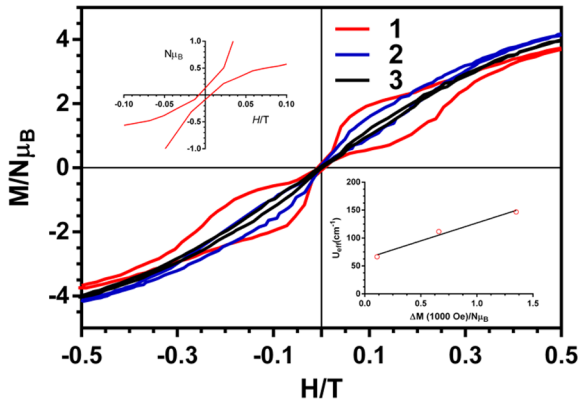

Figure 11. Magnetic hysteresis loops for compounds **1**−**3** within −5 kOe < H < 5 kOe at 2 K. The top left inset highlights the magnetic hysteresis of **1** at zero field, whereas the bottom right inset represents the linear relationship between U_{eff} and ΔM (M_{up} − M_{down}) at 1000 Oe.

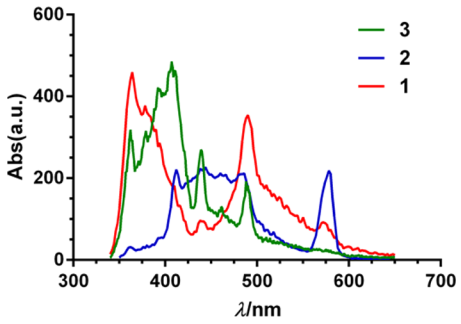

Figure 12. Sensitized emission spectra of complexes **1**−**3** in the solid state at room temperature after excitation at 330 nm.

large Mulliken negative charges on O atoms in complexes **2** and **3** (see Figures 10b and 10c). These O atoms create a strong crystal field and force the oblate electron density to be perpendicular to them, in order to minimize electrostatic repulsions, so that the anisotropy axis lies in the same direction of the axial crystal field.

Note that the experimental temperature dependence of the $\chi_M T$ product and the field dependence of the magnetization at 2 K can be both reasonably reproduced from the energy levels obtained in the *ab initio* calculations (see Figure 5 for **1** and Figures S1 and S2 for **2** and **3**, respectively), thus supporting the calculated low-lying state energies for **1**−**3**.

Furthermore, we have decided to investigate the relaxation mechanism underlying in these complexes. The magnetic relaxation in lanthanides are found to occur essentially because of three factors, in the absence of intermolecular interactions: (i) via QTM between the ground-state KDs, which is caused by the large transverse anisotropy of these states; (ii) via the Orbach/Raman process through the excited KDs (essentially occurring because of the noncoincidence of the principal anisotropic axes); and (iii) via thermally assisted QTM (TA-QTM) through the excited states, because of the non-Ising nature of the excited KDs. Qualitative mechanism of relaxation obtained from *ab initio* calculations for **1**, **2**, and **3** is shown in Figures 9d, 9e, and 9f, respectively. Here, the states are disposed following the values of their magnetic moments. The numbers shown in colors account for the mean absolute values of the matrix elements of the transition magnetic moments between the two states connected by the arrows. Pure Ising nature (g_z values of 19.94, 19.73, and 19.71 for **1**, **2**, and **3**, respectively) of ground-state anisotropy induces almost completely suppressed QTM (10^{-3} μ_B, 10^{-2} μ_B, and 10^{-2} μ_B for **1**, **2**, and **3**, respectively) in all three complexes.

For complexes **1** and **3**, the energy barrier is anticipated, with respect to the first excited KD (KD2), because of the large misalignment of the principal anisotropy axis (6.0° and 8.8° for **1** and **3**, respectively) of KD2, with respect to that of KD1. Hence, the calculated energy barrier for magnetization reversal is considered to be 177 and 131 cm^{-1} for **1** and **3**, respectively, in comparison to their experimental congeners of 82.9 and 44.3 cm^{-1}, respectively. This is subsequently corroborated by our appreciable magnitude of computed tunnelling between the excited states (TA-QTM as 10^{-1} μ_B order). Calculated overestimation of the energy barrier, if compared to the experimental values, can be ascribed to the limitations of the computational tool, which fails to consider either QTM between the ground-state KDs or intermolecular interactions. Experimental values closer to the calculated ones are extracted when either the QTM is taken into account in the fitting procedure or the QTM is suppressed by applying a small DC magnetic field of 1000 Oe.

For complex **2**, the huge transverse magnetic moment (0.21) between the first excited energy levels (KD2) implies the occurrence of TA-QTM through KD2. Besides, the moderate off-diagonal terms of the transversal magnetic moment between the ground state and first excited state (0.025) of opposite magnetization corresponds to the Orbach/Raman process and contributes to the overall relaxation phenomena. A spin phonon Orbach relaxation composed of direct/Raman process is most likely to occur via the first excited state (1.80) following the path $|-15/2\rangle \rightarrow |-13/2\rangle \rightarrow |+13/2\rangle \rightarrow |+15/2\rangle$. Contrary to this, almost collinear principal anisotropy axis of the first excited state (with respect to that of ground state; <3°, see Figure S9) may promote relaxation to levels further upward in

DOI: 10.1021/acs.inorgchem.6b00228
Inorg. Chem. 2016, 55, 4428−4440

order to spur the relaxation via second excited KD (KD3) [|−15/2⟩ → |−13/2⟩ → |−7/2⟩] → [|+7/2⟩ → |+13/2⟩ → |+15/2⟩] However, this would give rise to a calculated energy barrier for reorientation (U_{cal}) of magnetization of 229 cm^{-1}, which is much larger than the experimentally observed value (99.7 or 155 cm^{-1}, when the QTM is taken into account to extract U_{eff} at H_{dc} = 0). Hence, despite the collinearity of the principal magnetization axis of the KD2 level if compared to that of the ground state, major magnetic relaxation path is viable through the KD2 level. There is a minute chance for relaxation to move up further, to relax back to the equilibrium magnetization (as shown by thin lines in Figure 9e), only because of collinearity. This suggests that collinearity among the g_z-axis is not a sufficient condition to reach larger barrier heights and it is the axiality of the KDs, along with the collinearity, that dictates the relaxation barrier. In conclusion, our computed estimated barrier for **2** is 160 cm^{-1}.

The calculations reaffirm the axiality of the ground state in complex **2**, which predicted the ground state KD to be predominantly |±15/2⟩: 0.98|±15/2⟩, while the first excited state is strongly mixed |±13/2⟩: 0.73|±13/2⟩ + 0.32|±9/2⟩ (Remarkably, $\pm m_J$ notation in the relaxation mechanism plot is given based on the predominant contribution from $\pm m_J$ energy states). Retention of ground-state axiality for **1** and **3** is also reiterated by our computational values, which has predicted ground-state KD predominantly to be |±15/2⟩: 0.99|±15/2⟩ and KD2 preferentially as |±13/2⟩: 0.94|±13/2⟩ + 0.21 ±9/2⟩ for complex **1**, and KD1 preferably as |±15/2⟩: 0.98|±15/2⟩ and KD2 preferably as |±13/2⟩: 0.87|±13/2⟩ + 0.27 ±9/2⟩ in **3**.

The relaxation mechanism can be better understood by using computed crystal field parameters. The corresponding crystal field Hamiltonian is

$$\hat{H}_{CF} = \sum \sum_{k=-q}^{q} B_k^q \tilde{O}_k^q$$

where $\tilde{O}_k^q$ is the extended Stevens operator while B_k^q is the computed crystal field parameter (Table 3). The QTM contributions are negligible where the nonaxial B_k^q terms (where $k \neq 0$, and q = 2, 4, 6) are smaller than the axial B_k^q terms (where k = 0, and q = 2, 4, 6), which has been apparently proved by the magnitude of QTM observed in relaxation mechanism for all three complexes.

Finally, at 2 K and using the sweep rate accessible in a conventional SQUID magnetometer, compounds **1**−**3** exhibit butterfly-shaped hysteresis loops. Compound **1** displays a very small remnant magnetization (M_R = 0.135 Nμ_B) and coercive field (H_c = 75 Oe), while compounds **2** and **3** have negligible magnetization at zero field (see Figure 11). This behavior at zero-field reflects the QTM typically observed for lanthanide complexes and is consistent with the low-temperature tails found in the χ''_M vs T plots of **1**−**3** at zero applied field. Upon passing from compound **1** to compound **3**, the hysteresis at 1000 Oe decreases from 1.35 Nμ_B for **1**, to 0.66 Nμ_B for **2** and to 0.11 Nμ_B for **3**, which, as expected, agrees well with the decrease of their respective thermal energy barriers. In fact, there is a linear relationship between both parameters—hysteresis and $U_{eff.}$—at 1000 Oe.

Luminescence Properties. After excitation into the UV π−π^* absorption band of the ligands at 280 and 335 nm,[15] complexes **1** and **2** exhibit two metal-centered emission bands in the visible region at ∼485 nm and ∼575 nm, which corresponds with the characteristic emission $^4F_{9/2} \rightarrow {}^6H_J$ (J = 15/2, 13/2) transitions of the Dy^{3+} ion, respectively (Figure 12). This sensitized Ln^{III}-based emission can only occur through a Ligand → Ln photoinduced energy transfer process, which demonstrates the ability of the ligand L^{2-} to be active as an antenna group. However, an important remaining ligand-centered emission is still observed, which suggests that the energy is not fully transferred from the ligand to the lanthanide ion. A similar photoluminescence behavior has been observed for Zn−Dy−Zn trinuclear complexes containing the L^{2-} ligand. For compound **3**, the Dy^{III} emission bands are particularly very weak, compared to the emission band of the ligand $(L^1)^{2-}$, thus indicating that this ligand is a worse antenna group than L^{2-}. Interestingly, for compound **1**, the blue emission intensity of the $^4F_{9/2} \rightarrow {}^6H_{15/2}$ transition is much stronger than that of the yellow emission intensity of the $^4F_{9/2} \rightarrow {}^6H_{13/2}$ transition, whereas, for compound **2**, the intensity is reversed so that the yellow emission intensity seems to be slightly stronger that of the blue emission intensity of the $^4F_{9/2} \rightarrow {}^6H_{15/2}$ transition. This result suggests that L^{2-} is suitable for sensitization of the yellow luminescence of Dy^{3+}. This difference in luminescence behavior for **1** and **2** could be due to the effect of the different ligands coordinated to the Dy^{3+} in these compounds (*o*-vanillin vs diketone), which also can act as antenna groups.

Table 3. SINGLE-ANISO Computed Crystal Field Parameters for Complexes 1, 2, and 3[a]

H_{CF} Parameters[b]		B_k^q		
k value	q value	complex **1**	complex **2**	complex **3**
2	−2	−0.46	**−0.81 × 10^{-1}**	1.00
	−1	−0.29	0.65	−0.88
	0	−2.21	**−3.29**	**−3.23**
	1	−2.40	−1.51	−0.85
	2	**0.76**	2.25	0.30
4	−4	0.16 × 10^{-2}	0.41 × 10^{-2}	0.14 × 10^{-2}
	−3	**−0.55 × 10^{-3}**	−0.37 × 10^{-1}	−0.24 × 10^{-1}
	−2	**−0.42 × 10^{-2}**	0.12 × 10^{-1}	0.13 × 10^{-1}
	−1	0.52 × 10^{-2}	−0.57 × 10^{-2}	−0.28 × 10^{-2}
	0	−0.24 × 10^{-2}	**−0.16 × 10^{-2}**	**0.47 × 10^{-2}**
	1	0.28 × 10^{-1}	−0.11 × 10^{-1}	−0.92 × 10^{-2}
	2	**0.17 × 10^{-1}**	0.16 × 10^{-1}	−0.42 × 10^{-1}
	3	0.12 × 10^{-2}	−0.81 × 10^{-1}	−0.37 × 10^{-2}
	4	−0.79 × 10^{-2}	0.21 × 10^{-1}	−0.13 × 10^{-1}
6	−6	−0.16 × 10^{-4}	0.83 × 10^{-4}	0.87 × 10^{-4}
	−5	−0.11 × 10^{-2}	−0.13 × 10^{-4}	**−0.29 × 10^{-3}**
	−4	−0.11 × 10^{-3}	0.12 × 10^{-3}	0.38 × 10^{-5}
	−3	−0.15 × 10^{-4}	−0.77 × 10^{-4}	0.54 × 10^{-4}
	−2	0.17 × 10^{-4}	−0.30 × 10^{-4}	−0.67 × 10^{-4}
	−1	−0.57 × 10^{-4}	−0.48 × 10^{-4}	−0.16 × 10^{-3}
	0	−0.17 × 10^{-4}	**0.65 × 10^{-5}**	0.24 × 10^{-5}
	1	−0.19 × 10^{-3}	0.20 × 10^{-3}	0.11 × 10^{-4}
	2	−0.65 × 10^{-4}	−0.54 × 10^{-5}	0.19 × 10^{-3}
	3	−0.33 × 10^{-4}	−0.17 × 10^{-3}	0.25 × 10^{-3}
	4	−0.78 × 10^{-3}	0.35 × 10^{-4}	−0.39 × 10^{-4}
	5	**−0.75 × 10^{-3}**	−0.78 × 10^{-3}	−0.12 × 10^{-2}
	6	0.90 × 10^{-5}	−0.52 × 10^{-4}	−0.45 × 10^{-4}

[a]The major components in the table are shown in boldface font. [b]The quantization axis is chosen to be the main magnetic axes of the ground-state Kramer Doublet.

DOI: 10.1021/acs.inorgchem.6b00228
Inorg. Chem. 2016, 55, 4428−4440

CONCLUSIONS

Following the "complex-as-ligand" strategy and using the mononuclear Zn^{II} complexes $LZn{\cdot}2H_2O$ and $[L^1ZnBrNa]$ as building blocks to be assembled with the Dy^{III} ion and the corresponding bidentate ligands, we have succeeded in preparing a new dinuclear $Zn^{II}-Dy^{III}$ complex $[(LZnBrDy(ovan)(NO_3)(H_2O)](H_2O){\cdot}0.5(MeOH)$ (**1**) with double phenoxido bridging groups connecting Zn^{II} and Dy^{III} ions and a new cationic trinuclear Zn−Dy−Zn complex $[(L^1ZnBr)_2Dy(MeOH)_2](ClO_4)$ (**3**) with phenoxido/oximato bridging groups between each pair of Zn^{II} and Dy^{III} ions. In compound **1**, the Dy^{III} ion exhibits a DyO_9 coordination sphere, whereas in **3**, a DyO_8 coordination environment was observed. The magnetic properties and *ab initio* calculations were measured not only for **1** and **3**, but also for **2**, which is a complex previously reported by two of us;[18] it is similar to **1** but has two diketone bidentate ligands coordinated to the Dy^{III}, instead of bidentate *o*-vanilline and nitrate anions and where the bromide anion coordinated to Zn^{II} was replaced by chloride. *Ab initio* calculations on the crystal structures of these complexes indicate that (i) the pure Ising nature (g_z values of 19.94, 19.73, and 19.71 for **1**, **2**, and **3**, respectively) of the ground state, which induces almost completely suppressed QTM (10^{-3} μ_B, 10^{-2} μ_B, and 10^{-2} μ_B for **1**, **2**, and **3** respectively) in all three complexes and (ii) TA-QTM relaxations via the first excited-state Kramers doublet, leading to large energy barriers. Following these considerations, compounds **1**−**3** should exhibit SMM behavior. Alternating field susceptibility measurements clearly support the presence of zero-field SMM behavior with high thermal energy barriers for the reversal of the magnetization of 82.9, 69.3, and 44.3 cm^{-1} for **1**, **2**, and **3**, respectively. After applying a DC magnetic field of 1000 Oe, the QTM is partly or fully suppressed and the energy barriers increase to 146.7, 111.5, and 66.4 cm^{-1} for **1**, **2**, and **3**, respectively. The *ab initio*-calculated U_{eff} values (energy gap between the ground-state and first excited-state KDs) are overestimated (177.5, 159.9, and 131.3 cm^{-1} for **1**, **2**, and **3**, respectively) and follow the same trend as the experimental ones. Nevertheless, when either the QTM is taken into account in the fitting procedure or the QTM is suppressed by applying a small DC magnetic field of 1000 Oe, the experimental values are similar to those calculated above. This is due to the fact that the computed barrier heights are merely the energy gap between the KDs and do not factor in the QTM or intermolecular interactions.

Although the geometry of the O atoms around the Dy^{III} ion is one of the key factors that determine the magnitude of the experimental U_{eff} value, the larger U_{eff} value observed for **1**, compared to those of **2** and **3**, can be understood by only considering the presence of a Dy−O distance (Dy−O6 = 2.213 Å) that is significantly shorter (more than 0.1 Å) that the other ones, thus creating a large axial field, which is required to have a Ising ground state (M_J = ±15/2) and to observe a high U_{eff} value in Dy^{III} complexes. In complexes **2** and **3**, the differences between the shortest Dy−O bond distances are much smaller than in **1** and, consequently, the magnitude of the axial field. Nevertheless, in the DyO_8 coordination sphere of **2**, the mean value for the four shorter Dy−O distances (2.28 Å) is smaller than that for compound **3** (2.31 Å), which could favor, together with the geometry of the DyO_8 coordination sphere, a larger U_{eff} value for **2** than for **3**. Thus, the change of the *o*-vanillinato/nitrato bidentate ligands in **1** by two diketonate (thd) bidentate ligands in **2** leads to a decrease in the thermal energy barrier, mainly because the $Dy-O_{diketonate}$ bond distances are much longer that the shortest $Dy-O_{vanillinato}$ bond distance. Moreover, the U_{eff} value for compound **3** is smaller than that for the trinuclear $Zn^{II}-Dy^{III}-Zn^{II}$ complex $[(LZnBr)_2Dy(H_2O)](ClO_4)$ previously reported by us.[15] In view of this, it appears, in a crude manner, that the replacement of a phenoxide bridging group by a oxime bridging group in the Dy^{III} coordination sphere provokes a decrease in U_{eff}. Nevertheless, this conclusion must be taken with caution as the $[(LZnBr)_2Dy(H_2O)](ClO_4)$ complex presents a DyO_9 coordination sphere (in addition to eight O atoms from two ligands, a water molecule is coordinated to the Dy^{III} ion) instead of the DyO_8 coordination environment observed for **3**. Furthermore, the fact that the U_{eff} value at zero field for $[(LZnBr)_2Dy(H_2O)](ClO_4)$[15] is much larger than that of the dinuclear complex **1** suggests that the inclusion of additional Zn^{2+} ions could lead to an increase in U_{eff}. Nevertheless, this hypothesis must be treated with caution, because the geometry and magnitude of the axial ligand field around the Dy^{III} are different for **1** and $[(LZnBr)_2Dy(H_2O)](ClO_4)$.

According to the large thermal energy barrier and small QTM calculated and observed for compounds **1**−**3** (as revealed the tail at low temperature in the χ''_M vs T plot at zero applied field), they exhibit butterfly-shaped hysteresis loops at 2 K. Interestingly, only compound **1** (which exhibits the smaller calculated QTM at zero field) displays a very small remnant magnetization and coercive field at zero field. Note that there exists a linear relationship between the hysteresis at 1000 Oe and the value of U_{eff}, so that the former decreases as the latter decreases.

Finally, these SMMs exhibit metal- and ligand-centered emissions in the visible region, and, therefore, they can be considered as magnetoluminescent bifunctional molecular materials.

ASSOCIATED CONTENT

Supporting Information

The Supporting Information is available free of charge on the ACS Publications website at DOI: 10.1021/acs.inorgchem.6b00228.

Experimental and calculated temperature dependence of the magnetic susceptibility and field variation of the magnetization for complexes **2** and **3**. Temperature dependence of the in-phase AC susceptibility, variable temperature frequency dependence of the out-of-phase AC susceptibility, and Cole−Cole plots under DC fields of zero and 1000 Oe, orientations of the principal anisotropy directions (g_{zz}) for the eight calculated KDs, tables of the calculated energy spectrum, *g*-tensors, angle between the anisotropy axis of the excited and the ground state, and shape measures for **1**−**3** (PDF)

Crystallographic information for compound **1** (CIF)

Crystallographic information for compound **3** (CIF)

AUTHOR INFORMATION

Corresponding Authors

*E-mail: jean-pierre.costes@lcc-toulouse.fr (J.-P. Costes).

*E-mail: rajaraman@chem.iitb.ac.in (G. Rajaraman).

*E-mail: ecolacio@ugr.es (E. Colacio).

DOI: 10.1021/acs.inorgchem.6b00228
Inorg. Chem. 2016, 55, 4428−4440

Author Contributions

The manuscript was written through contributions of all authors. All authors have given approval to the final version of the manuscript.

Notes

The authors declare no competing financial interest.

■ ACKNOWLEDGMENTS

Financial support from the Spanish *Ministerio de Ciencia e Innovación* (MICINN) (Project No. CTQ2014-56312-P), the *Junta de Andalucía* (No. FQM-195, the Project of Excellence No. P11-FQM-7756) and the University of Granada. I.O. is grateful to the University of The Basque Country for a postdoctoral fellowship. The authors thank for technical and human support provided by SGIker Medidas Magneticas Gipuzkoa of UPV/EHU. G.R. would like to thank the DST (No. EMR/2014/000247) and DST Nanomission (No. SR/NM/NS-1119/2011) for funding. T.G. would like to thank UGC for an SRF fellowship.

■ REFERENCES

(1) Some reviews: (a) Gatteschi, D.; Sessoli, R.; Villain, J. *Molecular Nanomagnets*; Oxford University Press: Oxford, U.K., 2006. (b) Rinehart, J. D.; Long, J. R. *Chem. Sci.* **2011**, *2*, 2078−2085. (c) Guo, Y. N.; Xu, G. F.; Guo, Y.; Tang, J. *Dalton Trans.* **2011**, *40*, 9953−9963. (d) Sorace, L.; Benelli, C.; Gatteschi, D. *Chem. Soc. Rev.* **2011**, *40*, 3092−3104. (e) Luzon, J.; Sessoli, R. *Dalton Trans.* **2012**, *41*, 13556−13567. (f) Clemente-Juan, J. M.; Coronado, E.; Gaita-Ariño, A. *Chem. Soc. Rev.* **2012**, *41*, 7464−7478. (g) Woodruff, D. N.; Winpenny, R. E. P.; Layfield, R. A. *Chem. Rev.* **2013**, *113*, 5110−5148. (h) Zhang, P.; Guo, Y.-N.; Tang, J. *Coord. Chem. Rev.* **2013**, *257*, 1728−1763. (i) Layfield, R. A., Murugesu, M., Eds. *Lanthanides and Actinides in Molecular Magnetism*; Wiley−VCH: Weinheim, Germany, 2015. (j) Tang, J.; Zhang, P. *Lanthanide Single Molecule Magnets*; Springer−Verlag: Berlin, Heidelberg, 2015. (k) Habib, F.; Murugesu, M. *Chem. Soc. Rev.* **2013**, *42*, 3278−3288. (l) Layfield, R. A. *Organometallics* **2014**, *33*, 1084−1099. (m) Wang, B. W.; Gao, S. *The Rare Earth Elements, Fundamental and Applications*; Atwood, D. A., Ed.; John Wiley and Sons: Hoboken, NJ, 2012. (n) Sessoli, R.; Powell, A. K. *Coord. Chem. Rev.* **2009**, *253*, 2328−2341. (o) Andruh, M.; Costes, J. P.; Diaz, C.; Gao, S. *Inorg. Chem.* **2009**, *48*, 3342−3359. (p) Brechin, E. K. *Dalton Trans.* **2010**, *39*, 20 (themed issue on "Molecular Magnets"). (q) Sharples, J. W.; Collison, D. *Coord. Chem. Rev.* **2014**, *260*, 1−20. (r) Rosado-Piquer, L.; Sañudo, E. C. *Dalton Trans.* **2015**, *44*, 8771−8780. (s) Craig, G. A.; Murrie, M. *Chem. Soc. Rev.* **2015**, *44*, 2135−2147. (t) Bartolomé, J.; Luis, F.; Fernández, J. F. *Molecular Magnets: Physics and Applications*, Ed. Springer−Verlag: Berlin, Heidelberg, 2014. (u) Aromí, G.; Brechin, E. K. *Struct. Bonding (Berlin)* **2006**, *122*, 1−67. (v) Bagai, R.; Christou, G. *Chem. Soc. Rev.* **2009**, *38*, 1011−1026.

(2) (a) Bogani, L.; Wernsdorfer, W. *Nat. Mater.* **2008**, *7*, 179−186. (b) Vincent, R.; Klyatskaya, S.; Ruben, M.; Wernsdorfer, W.; Balestro, F. *Nature* **2012**, *488*, 357−360. (c) Ganzhorn, M.; Klyatskaya, S.; Ruben, M.; Wernsdorfer, W. *Nat. Nanotechnol.* **2013**, *8*, 165−169. (d) Jenkins, M.; Hümmer, T.; Martínez-Pérez, M. J.; García-Ripoll, J.; Zueco, D.; Luis, F. *New J. Phys.* **2013**, *15*, 095007. (e) Dediu, V. A.; Hueso, L. E.; Bergenti, I.; Taliani, C. *Nat. Mater.* **2009**, *8*, 707−716. (f) Prezioso, M.; Riminucci, A.; Graziosi, P.; Bergenti, I.; Rakshit, R.; Cecchini, R.; Vianelli, A.; Borgatti, F.; Haag, N.; Willis, M.; Drew, A. J.; Gillin, W. P.; Dediu, V. A. *Adv. Mater.* **2013**, *25*, 534−538. (g) Mannini, M.; Pineider, F.; Danieli, C.; Totti, F.; Sorace, L.; Sainctavit, P.; Arrio, M.-A.; Otero, E.; Joly, L.; Cezar, J. C.; Cornia, A.; Sessoli, R. *Nature* **2010**, *468*, 417−421. (h) Thiele, S.; Balestro, F.; Ballou, R.; Klyatskaya, S.; Ruben, M.; Wernsdorfer, W. *Science* **2014**, *344*, 1135−1138.

(3) (a) Rocha, A. R.; García-Suárez, V. M.; Bailey, S. W.; Lambert, C. J.; Ferrer, J.; Sanvito, S. *Nat. Mater.* **2005**, *4*, 335−339. (b) Affronte, M. *J. Mater. Chem.* **2009**, *19*, 1731−1737.

(4) Sessoli, R.; Boulon, M.-E.; Caneschi, A.; Mannini, M.; Poggini, L.; Wilhelm, F.; Rogalev, A. *Nat. Phys.* **2014**, *11*, 69−74.

(5) (a) Leuenberger, M. N.; Loss, D. *Nature* **2001**, *410*, 789−793. (b) Ardavan, A.; Rival, O.; Morton, J. J. L.; Blundell, S. J.; Tyryshkin, A. M.; Timco, G. A.; Winpenny, R. E. P. *Phys. Rev. Lett.* **2007**, *98*, 057201-1−057201-4. (c) Stamp, P. C. E.; Gaita-Ariño, A. *J. Mater. Chem.* **2009**, *19*, 1718−1730. (d) Martínez-Pérez, M. J.; Cardona-Serra, S.; Schlegel, C.; Moro, F.; Alonso, P. J.; Prima-García, H.; Clemente-Juan, J. M.; Evangelisti, M.; Gaita-Ariño, A.; Sesé, J.; Van Slageren, J.; Coronado, E.; Luis, F. *Phys. Rev. Lett.* **2012**, *108*, 247213-1−247213-5.

(6) (a) Neese, F.; Pantazis, D. A. *Faraday Discuss.* **2011**, *148*, 229−238. (b) Waldmann, O. *Inorg. Chem.* **2007**, *46*, 10035−10037.

(7) (a) Milios, C. J.; Vinslava, A.; Wernsdorfer, W.; Moggach, S.; Parsons, S.; Perlepes, S. P.; Christou, G.; Brechin, E. K. *J. Am. Chem. Soc.* **2007**, *129*, 2754−2755. (b) Inglis, R.; Taylor, S. M.; Jones, L. F.; Papaefstathiou, G. S.; Perlepes, S. P.; Datta, S.; Hill, S.; Wernsdorfer, W.; Brechin, E. K. *Dalton Trans.* **2009**, 9157−9168.

(8) Zadrozny, J. M.; Xiao, D. J.; Atanasov, M.; Long, G. J.; Grandjean, F.; Neese, F.; Long, J. R. *Nat. Chem.* **2013**, *5*, 577−581.

(9) Mondal, K. C.; Sundt, A.; Lan, Y.; Kostakis, G. E.; Waldmann, O.; Ungur, L.; Chibotaru, L. F.; Anson, C. E.; Powell, A. K. *Angew. Chem., Int. Ed.* **2012**, *51*, 7550−7554.

(10) (a) Langley, S. K.; Wielechowski, D. P.; Vieru, V.; Chilton, N. F.; Moubaraki, B.; Chibotaru, L. F.; Murray, K. S.; Abrahams, B. F. *Angew. Chem., Int. Ed.* **2013**, *52*, 12014−12019. (b) Hołyńska, M.; Premužić, D.; Jeon, I.-R.; Wernsdorfer, W.; Clérac, R.; Dehnen, S. *Chem.—Eur. J.* **2011**, *17*, 9605−9610.

(11) Ganivet, C. R.; Ballesteros, B.; De la Torre, G.; Clemente-Juan, J. M.; Coronado, E.; Torres, T. *Chem.—Eur. J.* **2013**, *19*, 1457−1465.

(12) (a) Rinehart, J. D.; Fang, M.; Evans, W. J.; Long, J. R. *Nat. Chem.* **2011**, *3*, 538−542. (b) Rinehart, J. D.; Fang, M.; Evans, W. J.; Long, J. R. *J. Am. Chem. Soc.* **2011**, *133*, 14236−14239.

(13) Langley, S. K.; Wielechowski, D. P.; Vieru, V.; Chilton, N. F.; Moubaraki, B.; Chibotaru, L. F.; Murray, K. S. *Chem. Sci.* **2014**, *5*, 3246−3256.

(14) (a) Watanabe, A.; Yamashita, A.; Nakano, M.; Yamamura, T.; Kajiwara, T. *Chem.—Eur. J.* **2011**, *17*, 7428−7432. (b) Liu, J.-L.; Chen, Y.-C.; Zheng, Y.-Z.; Lin, W.-Q.; Ungur, L.; Wernsdorfer, W.; Chibotaru, L. F.; Tong, M.-L. *Chem. Sci.* **2013**, *4*, 3310−3316. (c) Titos-Padilla, S.; Ruiz, J.; Herrera, J. M.; Brechin, E. K.; Wersndorfer, W.; Lloret, F.; Colacio, E. *Inorg. Chem.* **2013**, *52*, 9620−9626. (d) Zhu, Y. Y.; Cui, C.; Zhang, Y. Q.; Jia, J. H.; Guo, X.; Gao, C.; Qian, K.; Jiang, S. D.; Wang, B. W.; Wang, Z. M.; Gao, S. *Chem. Sci.* **2013**, *4*, 1802−1806. (e) Chandrasekhar, V.; Dey, A.; Mota, A. J.; Colacio, E. *Inorg. Chem.* **2013**, *52*, 4554−4561. (f) Upadhyay, A.; Singh, S. K.; Das, C.; Mondol, R.; Langley, S. K.; Murray, K. S.; Rajaraman, G.; Shanmugam, M. *Chem. Commun.* **2014**, *50*, 8838−8841. (g) Oyarzabal, I.; Ruiz, J.; Seco, J. M.; Evangelisti, M.; Camón, A.; Ruiz, E.; Aravena, D.; Colacio, E. *Chem.—Eur. J.* **2014**, *20*, 14262−14269. (h) Das, S.; Bejoymohandas, K. S.; Dey, A.; Biswas, S.; Reddy, M. L. P.; Morales, R.; Ruiz, E.; Titos-Padilla, S.; Colacio, E.; Chandrasekhar, V. *Chem.—Eur. J.* **2015**, *21*, 6449−6464. (i) Funes, A. V.; Carrella, L.; Rentschler, E.; Alborés, P. *Dalton Trans.* **2014**, *43*, 2361−2364. (j) Oyarzabal, I.; Ruiz, J.; Ruiz, E.; Aravena, D.; Seco, J. M.; Colacio, E. *Chem. Commun.* **2015**, *51*, 12353−12356.

(15) Costes, J. P.; Titos-Padilla, S.; Oyarzabal, I.; Gupta, T.; Duhayon, C.; Rajaraman, G.; Colacio, E. *Chem.—Eur. J.* **2015**, *21*, 15785−15796.

(16) Costes, J. P.; Dahan, F.; Wernsdorfer, W. *Inorg. Chem.* **2006**, *45*, 5−7.

(17) Costes, J. P.; Dahan, F.; Dupuis, A.; Laurent, J. P. *New J. Chem.* **1997**, *21*, 1211−1217.

(18) El Rez, B.; Costes, J. P.; Duhayon, C.; Vendier, L.; Sutter, J. P. *Polyhedron* **2015**, *89*, 213−218.

DOI: 10.1021/acs.inorgchem.6b00228
Inorg. Chem. 2016, 55, 4428−4440

(19) *Xcalibur CCD system, CrysAlisPro Software system, Version 1.171.35.19*; Agilent Technologies UK, Ltd.: Oxford, U.K., 2011.
(20) *CrysAlis CCD, CrysAlis RED and associated programs*; Oxford Diffraction, Ltd.: Abingdon, England, 2006.
(21) *SAINT*; Bruker AXS, Inc.; Madison, WI, USA, 2007.
(22) Palatinus, L.; Chapuis, G. *J. Appl. Crystallogr.* **2007**, *40*, 786−790.
(23) Betteridge, P. W.; Carruthers, J. R.; Cooper, R. I.; Prout, K.; Watkin, D. J. *J. Appl. Crystallogr.* **2003**, *36*, 1487.
(24) *International Tables for X-ray Crystallography*, Vol. *IV*; Kynoch Press: Birmingham, England, 1974.
(25) van der Sluis, P.; Spek, A. L. *Acta Crystallogr., Sect. A: Found. Crystallogr.* **1990**, *A46*, 194−201.
(26) Watkin, D. J.; Prout, C. K.; Pearce, L. J. *Cameron*; Chemical Crystallography Laboratory: Oxford, England, 1996.
(27) (a) Duncan, J. A. *J. Am. Chem. Soc.* **2009**, *131*, 2416−2416. (b) Aquilante, F.; De Vico, L.; Ferre, N.; Ghigo, G.; Malmqvist, P.-A.; Neograd y, P.; Pedersen, T. B.; Pitonak, M.; Reiher, M.; Roos, B. O.; Serrano-Andres, L.; Urban, M.; Veryazov, V.; Lindh, R. *J. Comput. Chem.* **2010**, *31*, 224−247. (c) Veryazov, V.; Widmark, P. O.; Serrano-Andres, L.; Lindh, R.; Roos, B. O. *Int. J. Quantum Chem.* **2004**, *100*, 626−635. (d) Karlström, G.; Lindh, R.; Malmqvist, P. A.; Roos, B. O.; Ryde, U.; Veryazov, V.; Widmark, P. O.; Cossi, M.; Schimmelpfennig, B.; Neograd y, P.; Seijo, L. *Comput. Mater. Sci.* **2003**, *28*, 222−239.
(28) Malmqvist, P. A.; Roos, B. O.; Schimmelpfennig, B. *Chem. Phys. Lett.* **2002**, *357*, 230−240.
(29) Chibotaru, L. F.; Ungur, L. J. *J. Chem. Phys.* **2012**, *137*, 064112-1−064112-22.
(30) (a) Langley, S. K.; Ungur, L.; Chilton, N. F.; Moubaraki, B.; Chibotaru, L. F.; Murray, K. S. *Inorg. Chem.* **2014**, *53*, 4303−4315. (b) Habib, F.; Luca, O. R.; Vieru, V.; Shiddiq, M.; Korobkov, I.; Gorelsky, S. I.; Takase, M. K.; Chibotaru, L. F.; Hill, S.; Crabtree, R. H.; Murugesu, M. *Angew. Chem., Int. Ed.* **2013**, *52*, 11290−11293; *Angew. Chem.* **2013**, *125*, 11500−11503.
(31) Roos, B. O.; Lindh, R.; Malmqvist, P. A.; Veryazov, V.; Widmark, P. O.; Borin, A. C. *J. Phys. Chem. A* **2008**, *112*, 11431−11435.
(32) Llunell, M.; Casanova, D.; Cirera, J.; Bofill, J. M.; Alemany, P.; Alvarez, S.; Pinsky, M.; Avnir, D. *SHAPE: Continuous shape measures of polygonal and polyhedral molecular fragments, Version 1.1b*; University of Barcelona and The Hebrew University of Jerusalem: Barcelona, Spain, 2005.
(33) Abragam, A.; Bleaney, B. *Electron Paramagnetic Resonance of Transition Ions*; Clarendon Press: Oxford, U.K., 1970.
(34) Shrivastava, K. N. *Phys. Status Solidi B* **1983**, *117*, 437−458.
(35) Chilton, N. F.; Collison, D.; McInnes, E. J. L.; Winpenny, R. E. P.; Soncini, A. *Nat. Commun.* **2013**, *4*, 2551.
(36) (a) Singh, S. K.; Gupta, T.; Rajaraman, G. *Inorg. Chem.* **2014**, *53*, 10835−10845. (b) Singh, S. K.; Gupta, T.; Shanmugam, M.; Rajaraman, G. *Chem. Commun.* **2014**, *50*, 15513−15516. (c) Gupta, T.; Rajaraman, G. *J. Chem. Sci.* **2014**, *126*, 1569−1579. (d) Singh, S. K.; Beg, M. F.; Rajaraman, G. *Chem.—Eur. J.* **2016**, *22*, 672−680.
(37) (a) Ruiz, J.; Lorusso, G.; Evangelisti, M.; Brechin, E. K.; Pope, S. J. A.; Colacio, E. *Inorg. Chem.* **2014**, *53*, 3586−3594. (b) Zhang, P.; Zhang, L.; Lin, S.-Y.; Tang, J. *Inorg. Chem.* **2013**, *52*, 6595−6602. (c) Yu, W.-R.; Lee, G.-H.; Yang, E.-C. *Dalton Trans.* **2013**, *42*, 3941−3949. (d) Towatari, M.; Nishi, K.; Fujinami, T.; Matsumoto, N.; Sunatsuki, Y.; Kojima, M.; Mochida, N.; Ishida, T.; Re, N.; Mrozinski, J. *Inorg. Chem.* **2013**, *52*, 6160−6178. (e) Palacios, M. A.; Titos-Padilla, S.; Ruiz, J.; Herrera, J. M.; Pope, S. J. A.; Brechin, E. K.; Colacio, E. *Inorg. Chem.* **2014**, *53*, 1465−1474. (f) Ehama, K.; Ohmichi, Y.; Sakamoto, S.; Fujinami, T.; Matsumoto, N.; Mochida, N.; Ishida, T.; Sunatsuki, Y.; Tsuchimoto, M.; Re, N. *Inorg. Chem.* **2013**, *52*, 12828−12841. (g) Maeda, M.; Hino, S.; Yamashita, K.; Kataoka, Y.; Nakano, M.; Yamamura, T.; Kajiwara, T. *Dalton Trans.* **2012**, *41*, 13640−13648. (h) Burrow, C. E.; Burchell, T. J.; Lin, P. H.; Habib, F.; Wernsdorfer, W.; Clerac, R.; Murugesu, M. *Inorg. Chem.* **2009**, *48*, 8051−8053.

DOI: 10.1021/acs.inorgchem.6b00228
Inorg. Chem. 2016, 55, 4428−4440